coatings

MDPI

Article

Photoluminescent and Photocatalytic Properties of Eu^{3+}-Doped MgAl Oxide Coatings Formed by Plasma Electrolytic Oxidation of AZ31 Magnesium Alloy

Stevan Stojadinović [1,2,*], Nenad Radić [3] and Rastko Vasilić [1]

[1] Faculty of Physics, University of Belgrade, Studentski trg 12–16, 11000 Belgrade, Serbia
[2] Faculty of Forestry, University of Belgrade, Kneza Višeslava 1, 11000 Belgrade, Serbia
[3] IChTM-Department of Catalysis and Chemical Engineering, University of Belgrade, Njegoševa 12, 11000 Belgrade, Serbia
* Correspondence: sstevan@ff.bg.ac.rs; Tel.: +381-11-7158161

Abstract: The synthesis of Eu^{3+}-doped MgAl oxide coatings containing MgO and $MgAl_2O_4$ was accomplished through plasma electrolytic oxidation of AZ31 magnesium alloy in aluminate electrolyte with the addition of Eu_2O_3 particles in various concentrations. Their morphological, structural, and above all, photoluminescent (PL) and photocatalytic activity (PA) were thoroughly investigated. PL emission spectra of MgAl oxide coatings feature characteristic emission peaks, which are ascribed to f–f transitions of Eu^{3+} ions from excited level $^5D_0$ to lower levels ^7F_J. The charge transfer state of Eu^{3+} or direct excitation of the Eu^{3+} ground state $^7F_0$ into higher levels of the 4f-manifold are both attributed to the PL peaks that appear in the excitation PL spectra of the obtained coatings. The fact that the transition $^5D_0 \rightarrow {}^7F_2$ (electrical dipole transition) in Eu^{3+}-doped MgAl oxide coatings is considerably stronger than the transition $^5D_0 \rightarrow {}^7F_1$ (magnetic dipole transition) indicates that Eu^{3+} ions occupied sites with non-inversion symmetry. Because of oxygen vacancy formation, the Eu^{3+}-doped MgAl oxide coatings had a higher PA in the degradation of methyl orange than the pure MgAl oxide coating. The highest PA was found in Eu^{3+}-doped MgAl oxide coating formed in an aluminate electrolyte with 4 g/L of Eu_2O_3 particles. The PA, morphology, and phase of Eu^{3+}-doped MgAl oxide coatings did not change after several consecutive runs, indicating outstanding stability of these photocatalysts.

Keywords: plasma electrolytic oxidation; photocatalysis; photoluminescence; MgO; $MgAl_2O_4$; Eu^{3+}

Citation: Stojadinović, S.; Radić, N.; Vasilić, R. Photoluminescent and Photocatalytic Properties of Eu^{3+}-Doped MgAl Oxide Coatings Formed by Plasma Electrolytic Oxidation of AZ31 Magnesium Alloy. *Coatings* **2022**, *12*, 1830. https://doi.org/10.3390/coatings12121830

Academic Editor: Francesco Ruffino

Received: 3 November 2022
Accepted: 25 November 2022
Published: 26 November 2022

1. Introduction

Magnesium alloys are commonly used in the aircraft, automotive, military, medical, and electronic industries [1–3]. However, because of their high chemical reactivity, magnesium alloys are prone to corrosion, limiting their use in corrosive environments [4,5]. Surface modification is widely recognized as the most prevalent method for improving a magnesium alloy's surface properties. A coating layer can enhance the corrosion resistance of the metallic substrate by acting as a barrier between the substrate and the environment [6–8]. Recently, many research groups have been investigating the plasma electrolytic oxidation (PEO) process as a surface-protective treatment for magnesium alloys [9–14].

PEO is a high-efficiency, low-priced, and environmentally friendly process for producing multicomponent oxide coatings with numerous functions on lightweight metals or metallic alloys [15–17]. The incidence of micro-discharging on the metal surface, which is complemented by gas evolution, indicates that the PEO process is connected with plasma creation [18–20]. Many processes such as light and heat emission and electrochemical and plasma-chemical reactions occur at the micro-discharge sites as a result of the elevated local temperature and pressure. These processes are responsible for altering the structure, content, and morphology of the oxide coatings that are produced.

Despite numerous articles investigating PEO of magnesium alloys [21–24], there is a lack of data describing the formation of PEO coatings on magnesium alloys with intended application as photocatalytic or as photoluminescent materials [25]. In this study, we showed that MgO and $MgAl_2O_4$ phases are present in coatings formed by PEO of AZ31 magnesium alloy in aluminate electrolyte. $MgAl_2O_4$ has been identified as a matrix component for the preparation of very efficient photoluminescent materials [26,27], whereas both MgO and $MgAl_2O_4$ have been recognized as efficient materials in the photocatalytic degradation of organic pollutants due to high concentration of surface vacancies and other defects [28,29]. MgO- and $MgAl_2O_4$-photoluminescent and photocatalytic active materials have previously been synthesized in powder form, limiting their practical applications, particularly in the field of photocatalysis, due to the high cost of photocatalyst separation and recovery from suspension. Additionally, the easy aggregation of photocatalyst particles renders them unsuitable for use in flow systems.

The main goal of presented research was to synthesize Eu^{3+}-incorporated oxide coatings by PEO on AZ31 magnesium alloy in an aluminate electrolyte with the addition of Eu_2O_3 particles and to examine their photoluminescent and photocatalytic capabilities. Our recent investigation has showed that Eu^{3+}-doped PEO-based coatings on different substrates (Ti, Zr, Nb, Hf, Gd, Y, Zn) can be formed in electrolyte containing Eu_2O_3 [30–35]. Among various trivalent rare earth ions, the Eu^{3+} ion is most promising among light-emitting materials, exhibiting intense PL red emission under UV excitation due to the $^5D_0 \rightarrow {}^7F_2$ transition [36]. In addition, positive effects of Eu^{3+} ion doping on the photocatalytic capabilities of several materials have been described in the literature [37–39]. The only partially populated 4f orbital structure of Eu^{3+} ions is favorable for electron trapping, which boosts photocatalytic activity by decreasing charge carrier recombination.

2. Materials and Methods

In this research, an AZ31 magnesium alloy (96% Mg, 3% Al, 1% Zn, Alfa Aesar) plate was used as a substrate. The substrates were cut in rectangular pieces with dimensions of 25 mm × 10 mm × 0.81 mm and then ultrasonically cleaned with acetone, warm air stream dried, and covered with insulating resin, leaving only the 15 mm × 10 mm active surface exposed to the electrolyte. More details about the experimental setup can be found in [40]. PEO coatings were formed in an aluminate electrolyte (5 g/L $NaAlO_2$) with Eu_2O_3 particles added in concentrations up to 8 g/L. PEO was done for 10 min at 150 mA/cm^2 constant current density. The electrolyte was kept at a constant temperature of 20 ± 1 °C. Following the PEO procedure, the samples were rinsed with distilled water and air dried.

The structural and elemental analyses of the PEO coatings were carried out utilizing scanning electron microscope (SEM, JEOL 840A, Tokyo, Japan) with energy-dispersive X-ray spectroscopy (EDS, Oxford INCA, Abingdon, UK). A Rigaku Ultima IV diffractometer (XRD, Tokyo, Japan) equipped with a CuKα radiation source was used for phase identification of PEO coatings. The ultraviolet–visible diffusion reflectance spectra (DRS) were collected by a Shimadzu UV-3600 spectrophotometer (Tokyo, Japan) coupled with an integrating sphere. The spectrofluorometer (Horiba Jobin-Yvon Fluorolog FL3-22, Edison, NJ, USA) using a xenon lamp as radiation source was used to measure excitation and emission photoluminescence (PL) spectra at room temperature.

Under simulated solar radiation, photodegradation of methyl orange (MO) was investigated to probe the photocatalytic activity (PA) of formed coatings. In a 6.8 cm diameter open cylindrical thermostated pyrex glass reactor, a solution containing 8 mg/L of MO was kept in the dark for one hour to achieve absorption–desorption equilibrium. The concentration of MO remained nearly constant, indicating that MO adsorption was negligible. Following that, samples were exposed to the light of a 300 W incandescent lamp (Solimed BH Quarzlampen, Leipzig, Germany) placed 25 cm above the top surface of the solution. On the steel wire holder, the samples were placed 5 mm above the reactor bottom. PA was estimated by monitoring MO decomposition in selected time intervals after exposure to irradiation. A spectrophotometer (UV-Vis Thermo Electron Nicolet Evolution 500, Sitting-

bourne, England) was used to measure the MO concentration using the maximum MO absorption peak at 464 nm.

Free hydroxyl radicals (•OH) have high potential rate to photodegrade MO and other organic pollutants. To identify possible creation of •OH on irradiated PEO coatings, PL measurements were carried out using terephthalic acid, because it is observed that it reacts with •OH, thus producing extremely fluorescent 2-hydroxyterephthalic acid with a PL maximum positioned at 425 nm [41]. The PEO coatings were placed in reactor with 10 mL of 5×10^{-4} mol/L terephthalic acid, which was diluted in aqueous solution of 2×10^{-3} mol/L NaOH. After the irradiation, PL spectra of the solution in which the reaction took place were collected utilizing the spectrofluorometer under the excitation wavelength of 315 nm.

3. Results and Discussion

3.1. Morphology, Chemical, and Phase Composition of Eu-Doped MgAl Oxide Coatings

Figure 1 shows the top-surface morphology of coatings made in aluminate electrolyte with the addition of Eu_2O_3 particles. Obtained coatings are laced with a number of micro-discharging canals of changing diameter and areas formed by the freezing of molten materials between them. It can be also observed that the addition of Eu_2O_3 particles to aluminate electrolyte does not influence the surface morphology.

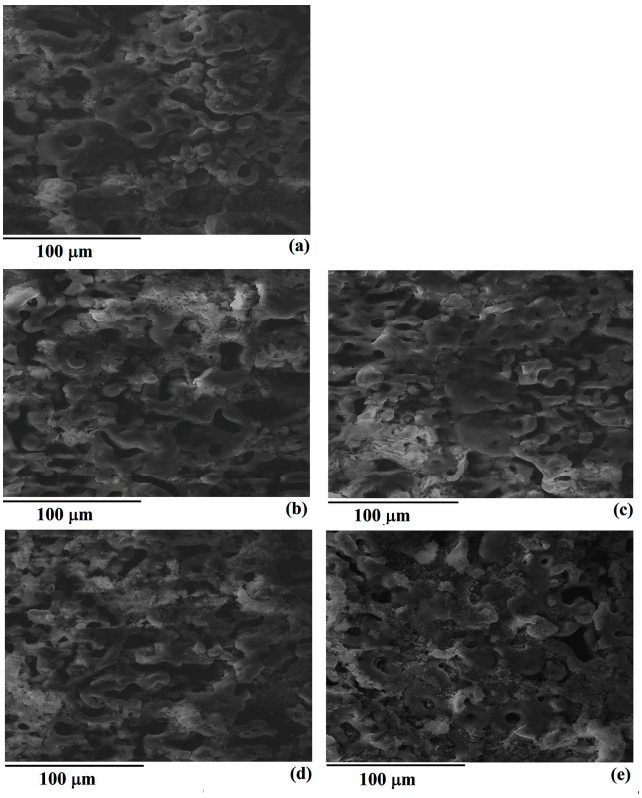

Figure 1. SEM micrographs of coatings obtained in aluminate electrolyte containing various additions of Eu_2O_3: (**a**) 0 g/L; (**b**) 2 g/L; (**c**) 4 g/L; (**d**) 6 g/L; (**e**) 8 g/L.

High temperatures which are inherent to PEO processing cause the melting of magnesium substrate, which enters the micro-discharging channels where it reacts with penetrated electrolyte. Products of these reactions, formed inside of micro-discharges, are ejected towards the oxide/electrolyte surface, where they promptly solidify upon contacting colder electrolyte. The repetition of these steps on a vast number of discrete locations where micro-discharging occurs results in thickening of the oxide coating. After 10 min of PEO, the formed coatings are roughly 22 μm thick and weakly dependent on the Eu_2O_3 particles' concentration in the aluminate electrolyte (Figure 2).

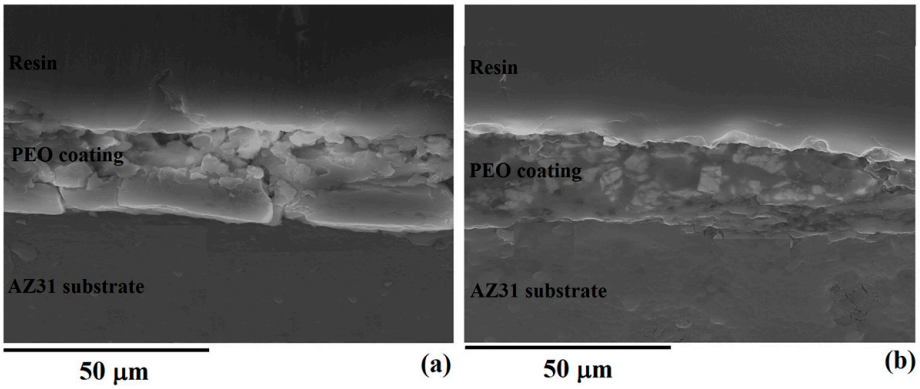

Figure 2. Cross-sections of coatings obtained in: (**a**) aluminate electrolyte; (**b**) aluminate electrolyte with 8 g/L of Eu_2O_3.

Table 1 presents the elemental composition of the coatings in Figure 1. The dominant elements in the coatings are Mg, Al, O, and Eu. The observed amount of Eu in coatings surges as the concentration of Eu_2O_3 in electrolyte increases. EDS elemental mapping reveals that observed elements are rather uniformly distributed in obtained coatings (Figure 3).

Table 1. EDS analysis of coatings in Figure 1.

Sample	Eu_2O_3 (g/L)	Atomic (%)			
		O	Mg	Al	Eu
Figure 1a	0	65.98	15.78	18.24	
Figure 1b	2	65.22	15.76	18.85	0.18
Figure 1c	4	65.35	16.02	18.21	0.41
Figure 1d	6	65.43	15.67	18.17	0.74
Figure 1e	8	64.96	16.44	17.67	0.92

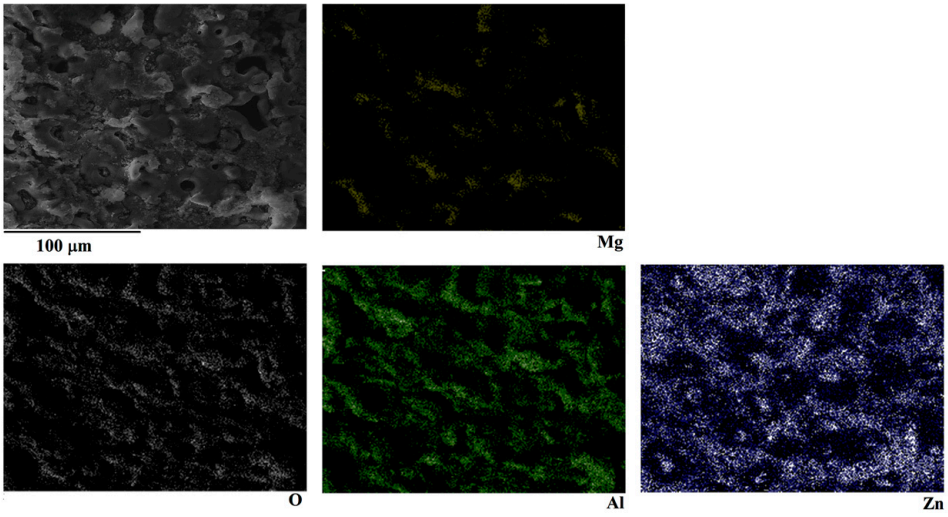

Figure 3. EDS maps of coating made in aluminate electrolyte with 8 g/L of Eu_2O_3.

The XRD patterns of pure Eu_2O_3 particles, AZ31 magnesium substrate, and formed coatings displayed in Figure 4. Observed diffraction patterns are characterized by XRD peaks that correspond to cubic phases of MgO (JCPDS card No. 79-0612) and $MgAl_2O_4$ (JCPDS card No. 77-0435). Diffraction peaks from the substrate are significant due to X-ray penetration through oxide coating and its reflection off the substrate. Despite the fact that elemental analysis confirmed the presence of Eu in the coatings, XRD analysis revealed no XRD maxima which can be attributed to Eu-containing crystalline phases.

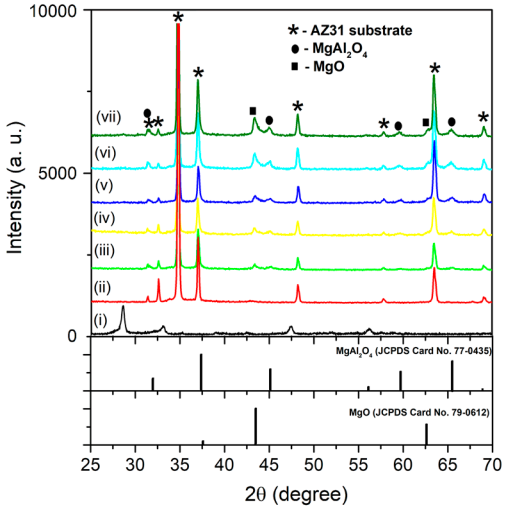

Figure 4. XRD patterns of: (**i**) Eu_2O_3 particles; (**ii**) AZ31 magnesium alloy; coatings formed in aluminate electrolyte with addition of: (**iii**) 0 g/L Eu_2O_3; (**iv**) 2 g/L Eu_2O_3; (**v**) 4 g/L Eu_2O_3; (**vi**) 6 g/L Eu_2O_3; (**vii**) 8 g/L Eu_2O_3.

The melting point of the Eu_2O_3 particles is around 2400 °C, which is considerably less than the estimated local temperature at the micro-discharging sites during PEO of AZ31 magnesium alloy [42]. Inside the micro-discharge channels, molten Eu_2O_3 particles can react with other components (originating either from substrate or from electrolyte) and participate in the formation of mixed-oxide coatings. The lack of diffraction peaks associated with Eu is most likely due to the uniform distribution of Eu throughout the surface coatings. It can also be observed that low Eu content in obtained coatings does not considerably change the crystalline structure of MgO and $MgAl_2O_4$.

3.2. PL of Eu^{3+}-Doped MgAl Oxide Coatings

The PL of MgAl oxide coatings with incorporated Eu is a combination of PL inherent to MgAl and Eu ions. PL excitation and emission spectra of MgAl oxide coating obtained in aluminate electrolyte are presented in Figure 5. The emission spectrum shows three dominant PL bands under ultraviolet excitation. The PL emission band centered at around 325 nm can be attributed to F^+ centers in MgO [40], while the PL band from 360 nm to 600 nm can be attributed to structural defects in the coating, such as Mg vacancies and interstitials [43,44]. The band with a maximum near 725 nm can be related to F^+ centers in $MgAl_2O_4$ [45].

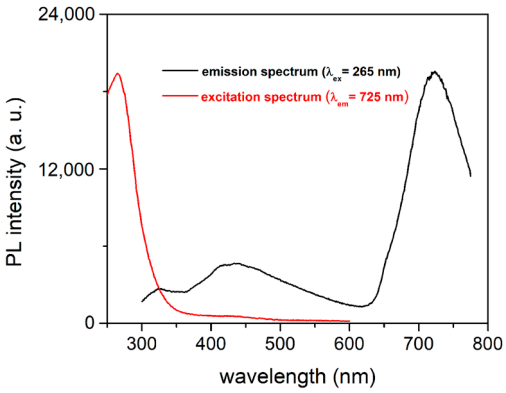

Figure 5. PL spectra of MgAl oxide coating formed in aluminate electrolyte.

The PL emission spectra of oxide coatings formed in aluminate electrolyte with varying concentration of Eu_2O_3 is presented in Figure 6a. Obviously, PL emission spectra

show two discrete regions: the first one contains a typical broad PL band of MgAl oxide coatings, whereas the second one contains well-defined PL emission bands intrinsic to Eu^{3+} 4f–4f transitions from the excited $^5D_0$ level to the lower ^7F_J levels (J = 0, 1, 2, 3, and 4) superimposed on PL of MgAl oxide coatings [36]. The PL bands are positioned at about 580 nm ($^5D_0 \rightarrow {}^7F_0$), 592 nm ($^5D_0 \rightarrow {}^7F_1$), 614 nm ($^5D_0 \rightarrow {}^7F_2$), 659 nm ($^5D_0 \rightarrow {}^7F_3$), and 708 nm ($^5D_0 \rightarrow {}^7F_4$). The intensity of the PL emission of 4f–4f transitions of Eu^{3+} increases as the concentration of Eu^{3+} in MgAl oxide coatings rises, indicating that the concentration of Eu^{3+} which is necessary for concentration quenching has not yet been reached.

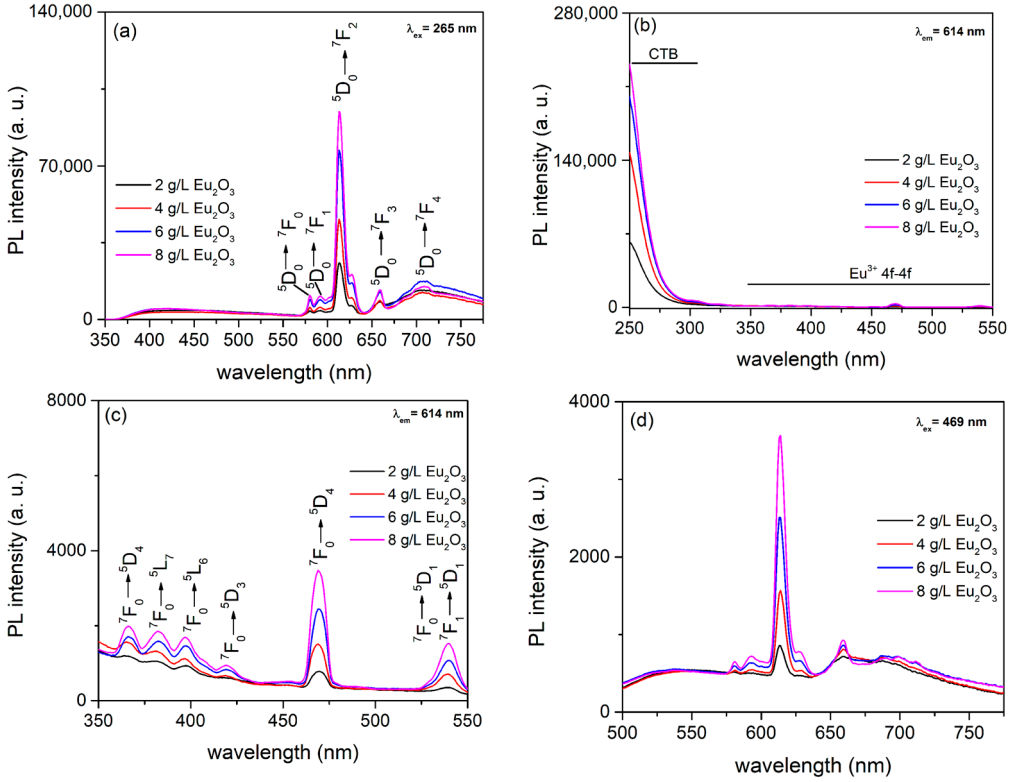

Figure 6. (**a**) PL emission spectra with 265 nm excitation; (**b**) PL excitation spectra monitored at 614 nm; (**c**) High-resolution PL excitation spectra monitored at 614 nm; (**d**) PL emission spectra with 469 nm excitation.

When PL excitation spectra are monitored at 614 nm (this wavelength corresponds to the most intense observed Eu^{3+} transition), an intense wide-ranging PL band in the region from 250 nm to 350 nm is observed (Figure 6b), which is followed by a series of narrow low-intensity bands (Figure 6c). Because the contribution of PL caused by optical transitions of MgAl oxide coatings is negligible, the broad PL band appears as a result of electron transfer between the fully occupied 2p orbital of O^{2-} and the incompletely occupied 4f orbital of the Eu^{3+} [46]. Sharp bands, as shown in Figure 6c, mostly correspond to direct excitation of the Eu^{3+} ground state $^7F_0$ into higher levels of the 4f-manifold [47]. The $^7F_0 \rightarrow {}^5D_2$ transition at 469 nm is the most intense of these excitation transitions and is used to record the PL emission spectra (Figure 6d).

When PL emission spectra are monitored under 469 nm excitation, typical narrow bands corresponding to the intra-configurational 4f–4f transitions of Eu^{3+} are observed. The intensity of the observed narrow band increases when the concentration of Eu^{3+} in MgAl oxide coatings increases, but the peak positions remain constant. Another interesting observation is the very high intensity of hypersensitive electric dipole transition $^5D_0 \rightarrow {}^7F_2$ at 614 nm compared to magnetic dipole transition $^5D_0 \rightarrow {}^7F_1$ at 592 nm. The electric dipole transition $^5D_0 \rightarrow {}^7F_2$ ($\Delta J = \pm 2$) is strongly dependent on changes in the environment around Eu^{3+} ions, while the magnetic dipole transition $^5D_0 \rightarrow {}^7F_1$ ($\Delta J = \pm 1$) does not depend on

the surrounding environment [36]. In other words, when Eu^{3+} ions are incorporated into non-inversion symmetry lattice sites, then $^5D_0 \rightarrow {}^7F_2$ electric dipole transition becomes dominant. In contrast, if Eu^{3+} ions are positioned at the inversion symmetry sites then the $^5D_0 \rightarrow {}^7F_1$ magnetic dipole transition becomes most prominent. In MgAl oxide coatings, the observed intensity of magnetic dipole transition is much lower than the corresponding intensity of electric dipole transition, suggesting that Eu^{3+} ions are positioned at non-inversion symmetry lattice sites.

The asymmetric ratio *R* between the transitions $^5D_0 \rightarrow {}^7F_2$ and $^5D_0 \rightarrow {}^7F_1$ provides information about the surroundings of incorporated Eu^{3+} ions. *R* values were calculated employing the equation [48]:

$$R = \frac{I(^5D_0 \rightarrow {}^7F_2)}{I(^5D_0 \rightarrow {}^7F_1)} \quad (1)$$

where $I(^5D_0 \rightarrow {}^7F_2)$ and $I(^5D_0 \rightarrow {}^7F_1)$ are the integrated intensities for the transitions $^5D_0 \rightarrow {}^7F_2$ (600 nm to 635 nm) and $^5D_0 \rightarrow {}^7F_1$ (585 nm to 600 nm), respectively. In MgAl oxide coatings, a high *R* value indicates an environment with a low degree of symmetry around the Eu^{3+} ions. Figure 7 clearly shows that an increase in Eu^{3+} concentration in the coatings results in higher R values, implying that increased concentration of Eu^{3+} in oxide coating results in lattice distortion and decreased symmetry around the Eu^{3+} ions. Because of differences in ionic radii between Eu^{3+} (95 pm), Mg^{2+} (66 pm), and Al^{3+} (51 pm), after replacing the Mg^{2+} or Al^{3+} ions, Eu^{3+} ions will create oxygen vacancies and cause the lattice distortion due to the size mismatch [49–51].

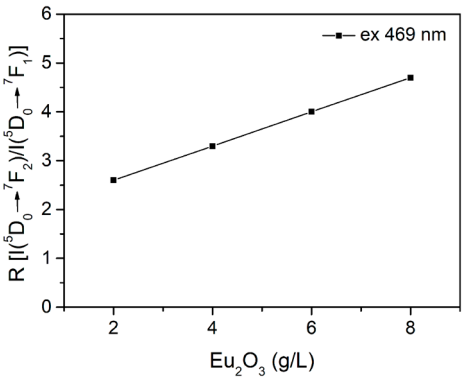

Figure 7. The asymmetric ratio between $^5D_0 \rightarrow {}^7F_2$ and $^5D_0 \rightarrow {}^7F_1$.

3.3. PA of Eu^{3+}-Doped MgAl Oxide Coatings

PA and optical absorption properties of pristine and Eu^{3+} doped MgAl oxide coatings formed by PEO processing of AZ31 in aluminate electrolyte with varying concentration of Eu_2O_3 are presented in Figure 8. As a result of the large bandgap between MgO [43] and $MgAl_2O_4$ [52], the broad absorption band in the mid-UV region is observed for MgAl oxide coatings. Although the MgAl coating's absorption band is detrimental for photocatalytic applications utilizing sunlight as the irradiation source, a high concentration of different types of oxygen vacancies and other defects generated in MgAl during the PEO processing results in good PA of MgAl coating. Because of the high concentration of surface vacancies, the PA of pure MgAl coating in MO degradation is considerably higher than that of commonly used TiO_2 [30], MgO [25], ZrO_2 [53], and Nb_2O_5 [54] coatings formed by PEO on titanium, AZ31 magnesium alloy, zirconium, and niobium substrates, respectively. Surface vacancies, which determine electron transfer between reactants and photocatalysts, were found to be closely related to active centers of heterogeneous photocatalytic reactions [55]. The PA of Eu^{3+}-doped MgAl oxide coatings is significant in comparison with pristine MgAl oxide coating (Figure 8a). Because the incorporation of Eu^{3+} ions into MgAl oxide coatings has no effect on their optical absorption in comparison to pristine MgAl oxide coating (Figure 8b), increased PA can be related to the interaction of Eu^{3+} ions and MgAl

oxide coatings. The incorporation of Eu^{3+} ions into MgAl oxide coatings during the PEO result in the formation of oxygen vacancy charge-trapping centers, which can lower the recombination rate of electrons and holes. As a result, Eu^{3+}-doped MgAl oxide coatings have higher PA than pure MgAl oxide coatings.

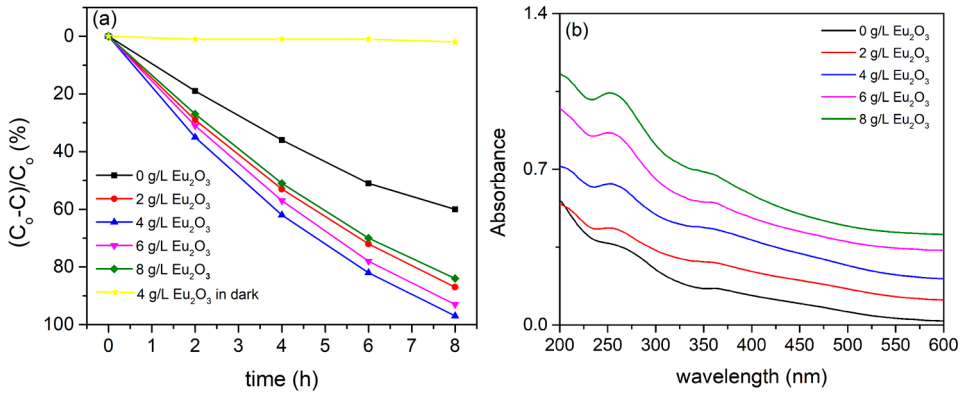

Figure 8. (**a**) PA and (**b**) DRS spectra of MgAl oxide coatings formed in aluminate electrolyte with varying concentration of Eu_2O_3 particles.

It can be clearly seen that PA is dependent on the concentration of Eu_2O_3 particles which are added to aluminate electrolyte, i.e., Eu^{3+} in MgAl oxide coatings. The PA of the Eu^{3+}-doped MgAl oxide coating formed in aluminate electrolyte with the addition of 4 g/L Eu_2O_3 is the highest, and it begins to decrease as the concentration of Eu_2O_3 particles increases. As a result, the most likely cause of PA decrease is that higher concentration of Eu^{3+} ions in MgAl oxide coatings increases the concentration of recombination centers for electron–hole pairs. Tests in the dark show that MO self-degradation is negligible.

Photo-generated electron–hole pairs formed on photocatalytic surfaces produce various active oxygen species such as the superoxide anion radical ($^{\bullet}O^{2-}$), hydrogen peroxide (H_2O_2), singlet oxygen ($^1O_2$), and the hydroxyl radical ($^{\bullet}OH$) [56]. $^{\bullet}OH$ radicals are primarily responsible for organic pollutants' degradation [57]. PL measurements performed in terephthalic acid on the surface of coatings formed in aluminate electrolyte with and without the addition of 4 g/L Eu_2O_3 particles are employed to test the formation of $^{\bullet}OH$ radicals. The quantity of produced $^{\bullet}OH$ radicals directly correlates with the intensity of PL [41]. Longer illumination times increase the PL intensity of both MgAl and Eu^{3+}-doped MgAl coatings, but the latter exhibits higher PL intensity at 425 nm emission (Figure 9). This observation is not surprising, since Eu^{3+}-doped MgAl coating shows higher PA.

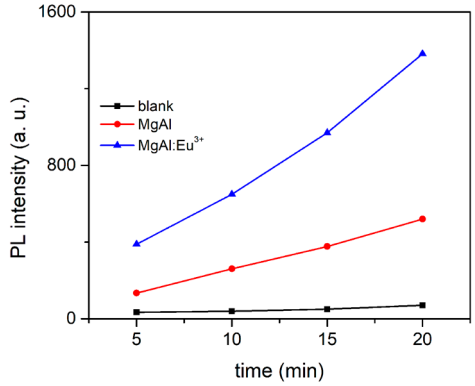

Figure 9. PL emission intensity monitored at 425 nm of terephthalic acid and coatings formed in aluminate electrolyte (MgAl) and aluminate electrolyte + 4 g/L Eu_2O_3 (MgAl:Eu^{3+}).

One of the most important requirements for the photocatalyst's applicability is its stability, which regulates the catalyst's lifetime and operating costs. The PA after five

consecutive runs using the most photocatalytically active formed coating is shown in Figure 10a. The sample was rinsed with water and dried between the runs. Figure 10a demonstrates that the PA did not decrease. Additionally, the morphology (Figure 10b) and phase structure (Figure 10c) did not change after five runs, proving the reliability and effectiveness of the Eu^{3+}-doped MgAl oxide coatings formed by PEO as photocatalysts.

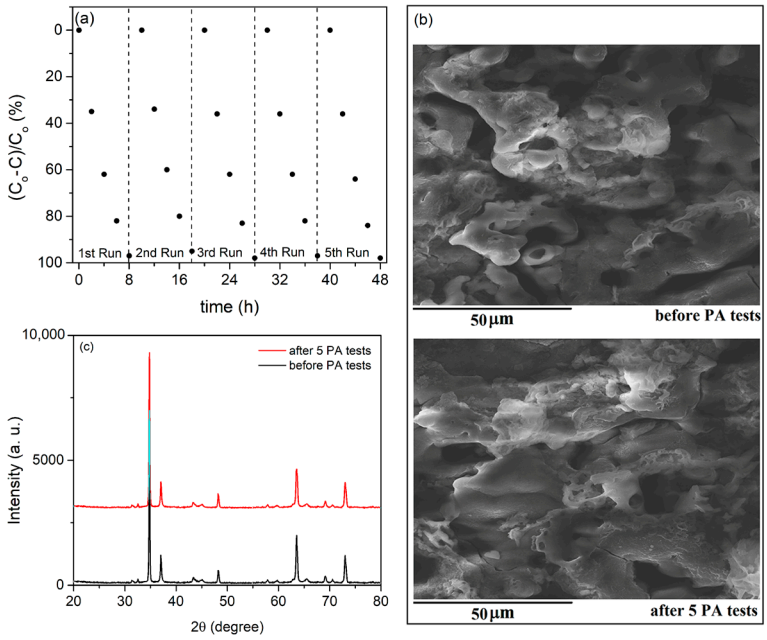

Figure 10. (**a**) Recycling PA test; (**b**) SEM micrographs before and after cycling; (**c**) XRD patterns before and after cycling.

4. Conclusions

In summary, Eu^{3+}-doped MgAl coatings were formed by plasma-electrolytic oxidation of AZ31 magnesium alloy in aluminate electrolyte which contains Eu_2O_3 particles. The coatings are crystallized and composed of MgO and $MgAl_2O_4$. DRS spectra of coatings exhibit a wide absorption band in the mid-UV region.

The emission PL spectra of Eu^{3+}-doped MgAl coatings display narrow emission bands, which are attributed to Eu^{3+} ion $^5D_0 \rightarrow {}^7F_J$ transitions. The excitation PL spectra of MgAl coatings doped with Eu^{3+} have a strong broad band which is related to the electron transfer transition from the 2p orbital of O^{2-} ions to the 4f orbital of Eu^{3+} ions followed by weak, well-defined peaks corresponding to direct excitation of the Eu^{3+} ground state $^7F_0$ into higher levels of the 4f-manifold. The electrical dipole transition $^5D_0 \rightarrow {}^7F_2$ is significantly stronger than the magnetic dipole transition $^5D_0 \rightarrow {}^7F_1$, indicating the presence of Eu^{3+} ions in an asymmetric environment.

The PA of MgAl coatings doped with Eu^{3+} is determined by the concentration of Eu_2O_3 particles in aluminate electrolyte, i.e., Eu^{3+} incorporated into MgAl coatings, with 4 g/L being the optimum Eu_2O_3 concentration in the aluminate electrolyte. Because the incorporation of Eu^{3+} particles into MgAl coatings has no significant effect on the absorption properties of formed coatings when compared to pure MgAl oxide coating, the increased PA of Eu^{3+}-doped MgAl coatings is due to the formation of oxygen vacancy charge-trapping centers, which reduces the recombination rate of electrons and holes.

Author Contributions: Conceptualization, S.S.; methodology, S.S.; validation, S.S., investigation, S.S., N.R. and R.V.; writing—original draft preparation, S.S.; writing—review and editing, S.S. and R.V. All authors have read and agreed to the published version of the manuscript.

Funding: This research was funded by the Ministry of Education, Science, and Technological Development of the Republic of Serbia (Grants 451-03-9/2021-14/200162 and 451-03-9/2021-14/200026)

and by the European Union Horizon 2020 Research and Innovation program under the Marie Sklodowska-Curie grant agreement No. 823942 (FUNCOAT).

Data Availability Statement: The data presented in this study are available on request from the corresponding author.

Conflicts of Interest: The authors declare no conflict of interest.

References

1. Mordike, B.L.; Ebert, T. Magnesium: Properties—applications—potential. *Mat. Sci. Eng. A* **2001**, *302*, 37–45. [CrossRef]
2. Ali, M.; Hussein, M.A.; Al-Aqeeli, N. Magnesium-based composites and alloys for medical applications: A review of mechanical and corrosion properties. *J. Alloys Compd.* **2019**, *792*, 1162–1190.
3. Ravichandran, N.; Mungara, S.R. Manufacturing and deployment of magnesium alloy parts for light weighting applications. Mater. *Today Proc.* **2021**, *47*, 4838–4843.
4. Liu, H.; Cao, F.; Song, G.-L.; Zheng, D.; Shi, Z.; Dargusch, M.S.; Atrens, A. Review of the atmospheric corrosion of magnesium alloys. *J. Mater. Sci. Technol.* **2019**, *35*, 2003–2016. [CrossRef]
5. Esmaily, M.; Svensson, J.E.; Fajardo, S.; Birbilis, N.; Frankel, G.S.; Virtanen, S.; Arrabal, R.; Thomas, S.; Johansson, L.G. Fundamentals and advances in magnesium alloy corrosion. *Prog. Mater. Sci.* **2017**, *89*, 92–193.
6. Daroonparvar, M.; Bakhsheshi-Rad, H.R.; Saberi, A.; Razzaghi, M.; Kasar, A.K.; Ramakrishna, S.; Menezes, P.L.; Misra, M.; Ismail, A.F.; Shariff, S.; et al. Surface modification of magnesium alloys using thermal and solid-state cold spray processes: Challenges and latest progresses. *J. Magnes. Alloys* **2022**, *10*, 2025–2061. [CrossRef]
7. Liu, Y.; Zhang, Y.; Wang, Y.-L.; Tian, Y.-Q.; Chen, L.-S. Research progress on surface protective coatings of biomedical degradable magnesium alloys. *J. Alloys Compd.* **2021**, *885*, 161001. [CrossRef]
8. Zhang, D.; Peng, F.; Liu, X. Protection of magnesium alloys: From physical barrier coating to\smart self-healing coating. *J. Alloys Compd.* **2021**, *853*, 157010. [CrossRef]
9. Lin, Z.; Wang, T.; Yu, X.; Sun, X.; Yang, H. Functionalization treatment of micro-arc oxidation coatings on magnesium alloys: A review. *J. Alloys Compd.* **2021**, *879*, 160453. [CrossRef]
10. Yao, W.; Wu, L.; Wang, J.; Jiang, B.; Zhang, D.; Serdechnova, M.; Shulha, T.; Blawert, C.; Zheludkevich, M.L.; Pan, F. Micro-arc oxidation of magnesium alloys: A review. *J. Mater. Sci. Technol.* **2022**, *118*, 158–180. [CrossRef]
11. Farshid, S.; Kharaziha, M. Micro and nano-enabled approaches to improve the performance of plasma electrolytic oxidation coated magnesium alloys. *J. Magnes. Alloys* **2021**, *9*, 1487–1504. [CrossRef]
12. Narayanan, T.S.N.S.; Park, I.S.; Lee, M.H. Strategies to improve the corrosion resistanceof microarc oxidation (MAO) coated magnesium alloys for degradable implants: Prospects and challenges. *Prog. Mater. Sci.* **2014**, *60*, 1–71. [CrossRef]
13. Chen, Y.; Lu, X.; Lamaka, S.V.; Ju, P.; Blawert, C.; Zhang, T.; Wang, F.; Zheludkevich, M.L. Active protection of Mg alloy by composite PEO coating loaded with corrosion inhibitors. *Appl. Surf. Sci.* **2020**, *504*, 144462. [CrossRef]
14. Fattah-alhosseini, A.; Chaharmahali, R.; Babaei, K. Effect of particles addition to solution of plasma electrolytic oxidation (PEO) on the properties of PEO coatings formed on magnesium and its alloys: A review. *J. Magnes. Alloys* **2020**, *8*, 799–818. [CrossRef]
15. Yerokhin, A.L.; Nie, X.; Leyland, A.; Matthews, A.; Dowey, S.J. Plasma electrolysis for surface engineering. *Surf. Coat. Technol.* **1999**, *122*, 73–93. [CrossRef]
16. Tsai, D.-S.; Chou, C.-C. Review of the soft sparking issues in plasma electrolytic oxidation. *Metals* **2018**, *8*, 105. [CrossRef]
17. Kaseem, M.; Fatimah, S.; Nashrah, N.; Ko, Y.G. Recent progress in surface modification of metals coated by plasma electrolytic oxidation: Principle, structure, and performance. *Prog. Mater. Sci.* **2021**, *117*, 100735. [CrossRef]
18. Stojadinović, S.; Vasilić, R.; Perić, M. Investigation of plasma electrolytic oxidation on valve metals by means of molecular spectroscopy—A review. *RSC Adv.* **2014**, *4*, 25759. [CrossRef]
19. Snizhko, L.O.; Yerokhin, A.L.; Pilkington, A.; Gurevina, N.L.; Misnyankin, D.O.; Leyland, A.; Matthews, A. Anodic processes in plasma electrolytic oxidation of aluminium in alkaline solutions. *Electrochim. Acta* **2004**, *49*, 2085–2095. [CrossRef]
20. Hussein, R.O.; Nie, X.; Northwood, D.O.; Yekokhin, A.; Matthews, A. Spectroscopic study of electrolytic plasma and discharging behaviour during the plasma electrolytic oxidation (PEO) process. *J. Phys. D* **2010**, *43*, 105203. [CrossRef]
21. Buling, A.; Zerrer, J. Increasing the application fields of magnesium by ultraceramic: Corrosion and wear protection by plasma electrolytical oxidation (PEO) of Mg alloys. *Surf. Coat. Technol.* **2019**, *369*, 142–155. [CrossRef]
22. Darband, G.B.; Aliofkhazraei, M.; Hamghalam, P.; Valizade, N. Plasma electrolytic oxidation of magnesium and its alloys: Mechanism, properties and applications. *J. Magnes. Alloys* **2017**, *5*, 74–132. [CrossRef]
23. Mashtalyar, D.V.; Nadaraia, K.V.; Plekhova, N.G.; Imshinetskiy, I.M.; Piatkova, M.A.; Pleshkova, A.I.; Kislova, S.E.; Sinebryukho, S.L.; Gnedenkov, S.V. Antibacterial Ca/P-coatings formed on Mg alloy using plasma electrolytic oxidation and antibiotic impregnation. *Mater. Lett.* **2022**, *317*, 132099. [CrossRef]
24. Rúa, J.M.; Zuleta, A.A.; Ramírez, J.; Fernández-Morales, P. Micro-arc oxidation coating on porous magnesium foam and its potential biomedical applications. *Surf. Coat. Technol.* **2019**, *360*, 213–221. [CrossRef]
25. Stojadinović, S.; Tadić, N.; Radić, N.; Grbić, B.; Vasilić, R. MgO/ZnO coatings formed on magnesium alloy AZ31 by plasma electrolytic oxidation: Structural, photoluminescence and photocatalytic investigation. *Surf. Coat. Technol.* **2017**, *310*, 98–105. [CrossRef]

26. Kumar, G.K.; Bhargav, P.B.; Aravinth, K.; Ahmed, N.; Balaji, C. Photoluminescence and electrochemical performance evaluation of Eu^{3+} doped $MgAl_2O_4$ phosphors for LED and energy storage applications. *Ceram. Int.* **2022**, *48*, 36038–36045. [CrossRef]
27. Golyeva, E.V.; Kolesnikov, I.E.; Lähderanta, E.; Kurochkin, A.V.; Mikhailov, M.D. Effect of synthesis conditions on structural, morphological and luminescence properties of $MgAl_2O_4$:Eu^{3+} nanopowders. *J. Lumin.* **2018**, *194*, 387–393. [CrossRef]
28. Cao, N.; Zhao, X.; Gao, M.; Li, Z.; Ding, X.; Li, C.; Liu, K.; Du, X.; Li, W.; Feng, J.; et al. Superior selective adsorption of MgO with abundant oxygen vacancies to removal and recycle reactive dyes. *Sep. Purif. Technol.* **2021**, *275*, 119236. [CrossRef]
29. Ball, J.A.; Murphy, S.T.; Grimes, R.W.; Bacorisen, D.; Smith, R.; Uberuaga, B.P.; Sickafus, K.E. Defect processes in $MgAl_2O_4$ spinel. *Solid State Sci.* **2008**, *10*, 717–724. [CrossRef]
30. Stojadinović, S.; Radić, N.; Grbić, B.; Maletić, S.; Stefanov, P.; Pačevski, A.; Vasilić, R. Structural, photoluminescent and photocatalytic properties of TiO_2:Eu^{3+} coatings formed by plasma electrolytic oxidation. *Appl. Surf. Sci.* **2016**, *370*, 218–228. [CrossRef]
31. Stojadinović, S.; Vasilić, R. Formation and photoluminescence of Eu3+ doped zirconia coatings formed by plasma electrolytic oxidation. *J. Lumin.* **2016**, *176*, 25–31. [CrossRef]
32. Stojadinović, S.; Vasilić, R. Orange–red photoluminescence of Nb_2O_5:Eu^{3+}, Sm^{3+} coatings formed by plasma electrolytic oxidation of niobium. *J. Alloys Compd.* **2016**, *685*, 881–889. [CrossRef]
33. Stojadinović, S.; Tadić, N.; Ćirić, A.; Vasilić, R. Photoluminescence properties of Eu^{3+} doped HfO_2 coatings formed by plasma electrolytic oxidation of hafnium. *Opt. Mater.* **2018**, *77*, 19–24. [CrossRef]
34. Ćirić, A.; Stojadinović, S.; Dramićanin, M.D. Luminescence temperature sensing using thin-films of undoped Gd_2O_3 and doped with Ho^{3+}, Eu^{3+} and Er^{3+} prepared by plasma electrolytic oxidation. *Ceram. Int.* **2020**, *46*, 23223–23231. [CrossRef]
35. Stojadinović, S.; Ćirić, A. Photoluminescence of ZnO:Eu^{3+} and ZnO:Tb^{3+} coatings formed by plasma electrolytic oxidation of pure zinc substrate. *J. Lumin.* **2021**, *235*, 118022. [CrossRef]
36. Binnemans, K. Interpretation of europium(III) spectra. *Coord. Chem. Rev.* **2015**, *295*, 1–45.
37. Kumar, M.; Singh, G.; Chauhan, M.S. Europium (Eu^{3+})—doped ZnO nanostructures: Synthesis, characterization, and photocatalytic, chemical sensing and preliminary assessment of magnetic properties. *Ceram. Int.* **2021**, *47*, 17023–17033. [CrossRef]
38. Huang, F.; Li, Z.; Yan, A.; Dong, H.; Li, Q.; Hu, M.; Xiong, X.; Gao, Q. Boosted visible-light photocatalytic activity and retarded carrier recombination of Eu3+-doped Nb3O7F nanomaterials prepared by hydrothermal method. *Nanotechnology* **2020**, *31*, 18520. [CrossRef] [PubMed]
39. Borlaf, M.; Moreno, R.; Ortiz, A.L.; Colomer, M.T. Synthesis and photocatalytic activity of Eu^{3+}-doped nanoparticulate TiO_2 sols and thermal stability of the resulting xerogels. *Mater. Chem. Phys.* **2014**, *144*, 8–16. [CrossRef]
40. Ćirić, A.; Stojadinović, S. Photoluminescence of ZrO_2:Gd^{3+} and ZrO_2:Dy^{3+} coatings formed by the plasma electrolytic oxidation. *J. Alloys Compd.* **2020**, *832*, 154907. [CrossRef]
41. Ishibashi, K.; Fujishima, A.; Watanabe, T.; Hashimoto, K. Detection of active oxidative species in TiO_2 photocatalysis using the fluorescence technique. *Electrochem. Commun.* **2000**, *2*, 207–210. [CrossRef]
42. Stojadinović, S.; Vasilić, R.; Radić-Perić, J.; Perić, M. Characterization of plasma electrolytic oxidation of magnesium alloy AZ31 in alkaline solution containing fluoride. *Surf. Coat. Technol.* **2015**, *273*, 1–11. [CrossRef]
43. Mageshwari, K.; Mali, S.S.; Sathyamoorthy, R.; Patil, P.S. Template-free synthesis of MgO nanoparticles for effective photocatalytic applications. *Powder Technol.* **2013**, *249*, 456–462. [CrossRef]
44. Jintakosol, T.; Singjai, P. Effect of annealing treatment on luminescence property of MgO nanowires. *Curr. Appl. Phys.* **2009**, *9*, 1288–1292. [CrossRef]
45. Pathak, N.; Ghosh, P.S.; Gupta, S.K.; Mukherjee, S.; Kadam, R.M.; Arya, A. An insight into the various defects-induced emission in $MgAl_2O_4$ and their tunability with phase behavior: Combined experimental and theoretical approach. *J. Phys. Chem. C* **2016**, *120*, 4016–4031. [CrossRef]
46. Lu, Y.; Wang, J.; Shi, Z.; Shi, J.; Liu, Y.; He, L. Site occupation and fluorescence properties of $MgAl_2O_4$: Eu^{3+} phosphors. *Mater. Sci. Semicond. Proc.* **2022**, *137*, 106233. [CrossRef]
47. Kolesnikov, I.E.; Golyeva, E.V.; Kurochkin, A.V.; Mikhailov, M.D. Structural and luminescence properties of $MgAl_2O_4$:Eu^{3+} nanopowders. *J. Alloys Compd.* **2016**, *654*, 32–38. [CrossRef]
48. Tanner, P.A. Some misconceptions concerning the electronic spectra of tri-positive europium and cerium. *Chem. Soc. Rev.* **2013**, *42*, 5090–5101. [CrossRef]
49. Guan, W.; Li, J.; Wang, X. Luminescence properties of Eu^{3+}-doped $MgAl_2O_4$ nanopowders synthesized by micro-emulsion method. *Phys. Status Solidi A* **2014**, *211*, 1778–1781. [CrossRef]
50. Reddy, G.K.; Krishna, R.H.; Reddy, A.J.; Monika, D.L.; Manjunath, C.; Prasanna Kumar, S.G.; Preetham, R.; Gopal, G.R. Facile self-propagating combustion synthesis of MgO:Eu^{3+} orangered nanophosphor and luminescence investigation by Judd-Ofelt intensity parameters. *Optik* **2018**, *174*, 234–243.
51. Wiglusz, R.J.; Grzyb, T.; Lis, S.; Strek, W. Hydrothermal preparation and photoluminescent properties of $MgAl_2O_4$:Eu^{3+} spinel nanocrystals. *J. Lumin.* **2010**, *130*, 434–441. [CrossRef]
52. Jagadeeshwaran, C.; Madhan, K.; Murugaraj, R. Size effect and order–disorder phase transition in $MgAl_2O_4$: Synthesized by co-precipitation method. *J. Mater. Sci. Mater. Electron.* **2018**, *29*, 18923–18934. [CrossRef]
53. Stojadinović, S.; Vasilić, R.; Radić, N.; Grbić, B. Zirconia films formed by plasma electrolytic oxidation: Photoluminescent and photocatalytic properties. *Opt. Mater.* **2015**, *40*, 20–25. [CrossRef]

54. Stojadinović, S.; Tadić, N.; Radić, N.; Stefanov, P.; Grbić, B.; Vasilić, R. Anodic luminescence, structural, photoluminescent, and photocatalytic properties of anodic oxide films grown on niobium in phosphoric acid. *Appl. Surf. Sci.* **2015**, *355*, 912–920. [CrossRef]
55. Wang, B.; Liu, J.; Yao, S.; Liu, F.; Li, Y.; He, J.; Lin, Z.; Huang, F.; Liu, C.; Wang, M. Vacancy engineering in nanostructured semiconductors for enhancing photocatalysis. *J. Mater. Chem. A* **2021**, *9*, 17143. [CrossRef]
56. Nosaka, Y.; Nosaka, A.Y. Generation and detection of reactive oxygen species in photocatalysis. *Chem. Rev.* **2017**, *117*, 11302–11336. [CrossRef] [PubMed]
57. Al-Mamun, M.R.; Kader, S.; Islam, M.S.; Khan, M.Z.H. Photocatalytic activity improvement and application of UV-TiO_2 photocatalysis in textile wastewater treatment: A review. *J. Environ. Chem. Eng.* **2019**, *7*, 103248. [CrossRef]